ACS Catalysis

Article

Oxygen Vacancy Structure Associated Photocatalytic Water Oxidation of BiOCl

Hao Li, Jian Shang, Huijun Zhu, Zhiping Yang, Zhihui Ai, and Lizhi Zhang

ACS Catal., **Just Accepted Manuscript** • DOI: 10.1021/acscatal.6b02613 • Publication Date (Web): 04 Nov 2016

Oxygen Vacancy Structure Associated Photocatalytic Water Oxidation of BiOCl

Hao Li, Jian Shang, Huijun Zhu, Zhiping Yang, Zhihui Ai, and Lizhi Zhang[*]

Key Laboratory of Pesticide & Chemical Biology of Ministry of Education, Institute of Environmental & Applied Chemistry, College of Chemistry, Central China Normal University, Wuhan 430079, P. R. China

[*]E-mail: zhanglz@mail.ccnu.edu.cn. Phone/Fax: +86-27-6786 7535

Abstract: A central issue in understanding the photocatalytic water splitting on stoichiometric or defective nanostructured oxide surface is its adsorption mode and related reactivity. More than just improving the adsorption of water on oxide surface, we demonstrate in this work that surface oxygen vacancies (OVs) also offer a possibility to activate water toward thermodynamically enhanced photocatalytic water oxidation, while the water activation state, as reflected by its capability to trap holes, strongly depends on the structures of OVs. Utilizing well-ordered BiOCl single-crystalline surfaces, we reveal that dissociatively adsorbed water on the OV of (010) surface exhibits higher tendency to be oxidized than the molecularly adsorbed one on the OV of (001) surface. Analysis of the geometric atom arrangement shows that the OV of BiOCl (010) surface can facilitate the barrierless O-H bond breaking in the first proton removal reaction, which is sterically hindered on the OV of BiOCl (001) surface, and also allow more localized electrons transfer from the OV to the dissociatively adsorbed water, leading to its higher water activation level for hole trapping. These findings highlight the indispensable role of crystalline surface structure on water oxidation, and may open up avenues for the rational design of highly efficient photocatalysts via surface engineering.

Keywords: Water oxidation; Photocatalysis; BiOCl; Oxygen vacancies; Facet dependency

Introduction

Water chemistry on oxide surfaces is of great significance for both scientific and fundamental applications including gas sensors, biomedical implants, batteries, fuel cells and heterogeneous catalysis. Of particular interest is the photocatalytic water oxidation on semiconducting oxide surfaces due to the urgent need for efficient environmental control and solar energy conversion, whose relevant chemical processes taking place on the surfaces involve water acting as both the

"spectator" (reaction medium) and the key participants.[1-4] Typically, photocatalytic water oxidation is initiated by the first proton removal reaction (H_2O^* + hole$^+$ → •OH* + H^+; the superscript * denotes the adsorbed state), which involves both the O-H bond breaking and the trapping of a photogenerated hole on the valence band (VB).[5-7] Diffusion of the •OH* species away from the surfaces allows the generation of free •OH radicals, which can be further coupled to generate H_2O_2. Both •OH radicals and H_2O_2 are the key components for the organic pollutants removal.[1] Also, •OH* species can be further oxidized to O_2 via multihole transfer process, leaving electrons on the conduction band (CB) capable of reducing H^+ or CO_2 for solar fuel production, or fixing N_2 for ammonia synthesis.[2,8-10]

Although the position of VB maximum, which determines the oxidizing capability of photogenerated holes, has been long believed to govern the thermodynamics of photocatalytic water oxidation, this point of view is not supported by recent theoretical and experimental results yet. For example, photocatalytic water oxidation on many prototypical stoichiometric TiO_2 surfaces is still thermodynamically unfavorable even though the position of VB is adequately matched with the water's oxidation potential. From the surface catalysis standpoint, such unfavorableness is mainly ascribed to the undesirable electronic state of surface-adsorbed water. Typically, surface coordinating unsaturated (5-coordinated) Ti cations provide the most reliable sites for water adsorption via the Lewis-Acid interaction. Such an interaction usually results in the donation of lone paired electrons from the O atom of adsorbed water to metal cations, decreasing the water's overall charge density. Consequently, this interfacial charge transfer behavior will drives the occupied states of adsorbed water lower than the upper edge of TiO_2 VB, impeding the transfer of photoinduced holes to adsorbed water thermodynamically.[11-15] In view of the strong adsorption mode dependent

water oxidation on semiconductor surfaces, a key strategy to enhance the thermodynamics of water oxidation is to regulate the water-surface interaction mode toward water activation for a better hole trapping.[15]

To realize this goal, we propose the introduction of native surface oxygen vacancies (OVs), because OVs can significantly influence the geometric structure and electronic structure of oxide surfaces, thus altering their chemical reactivity.[16,17] For the adsorption of inert molecules like O_2, N_2 and CO_2, OVs can act as the direct coordinating sites for enhanced substrates adsorption, and also as the charge donor sites capable of activating these molecules due to the abundant electrons localized at OVs.[18-22] To confirm whether water can be activated on the OVs with enhanced thermodynamics toward oxidation, BiOCl is selected as the model catalyst because its photoreactivity is closely related to OVs, which can be *in situ* generated under UV or solar light because the surface Bi-O bonds of long length and low energy are weak.[23,24] Besides, the successful preparation of two well-ordered, single crystalline surfaces allows the comparative study of water chemistry on OVs with different structures possible.[25]

Results and Discussion

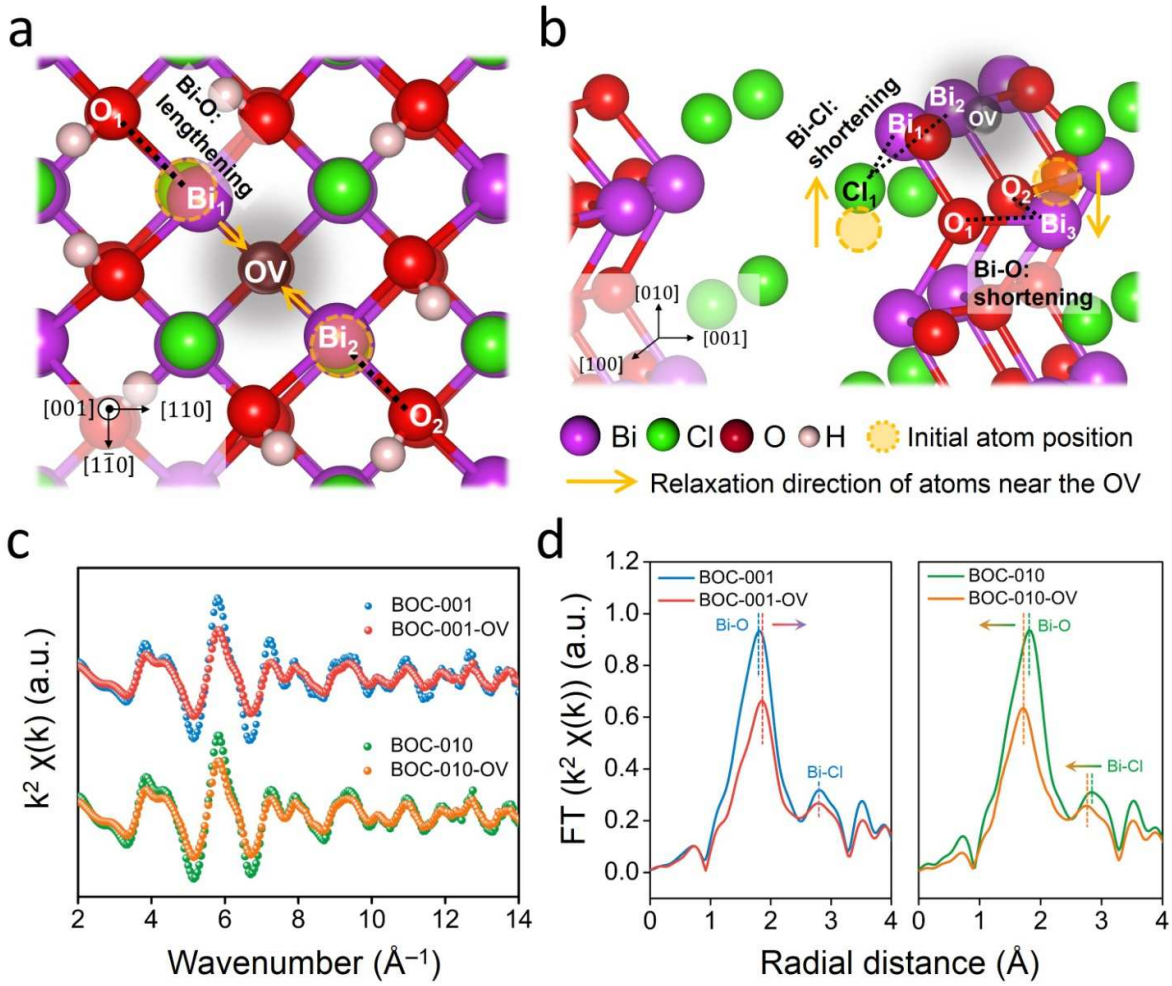

Figure 1. Surface structure of different BiOCl surfaces with OVs. Schematic illustration of the (a) in-plane and (b) out-plane relaxation over the atoms around the OV on the BiOCl (001) and (010) surfaces, respectively. (c) Bi L-edge extended XAFS oscillation function $k^2\chi(k)$ and (d) the corresponding Fourier transforms for the BiOCl with and without OVs.

The prototypical surfaces of BiOCl are the (001) and (010) surface, whose surface atom arrangements are different from each other. The (001) surface of BiOCl is of a close-packed structure with exposure of high density O atoms. As the protons in acid solution (pH = 1) during the synthesis of this surface are abundant, the adsorption of protons onto BiOCl (001) surface leads to

the formation of a layer of hydroxyl groups (Figure S1a).[26, 27] The (010) surface of BiOCl synthesized in near neutral solution possesses an open channel structure with O, Bi and Cl atoms exposed, in which the coordination of Bi atoms is unsaturated (Figure S1b). After the introduction of an OV on these two surfaces, local atoms around the OV suffered from a distinct geometrical distortion according to the density functional theory (DFT) calculation. Parallel to the (001) surface, two nearest Bi (Bi_1, Bi_2) atoms around the OV in the sublayer were relaxed toward the OV, lengthening the corresponding Bi_1-O_1 (or Bi_2-O_2) bond from 2.28 Å to 2.36 Å (Figures 1a and S2a). Differently, atoms relaxation perpendicular to the (001) surface was not observed and the average bond length of Bi-Cl around the OV did not change significantly (Figure S2b). We called this atoms relaxation behavior as in-plane relaxation. On the (010) surface, no atoms relaxed parallel to the (010) surface after the introduction of an OV (Figure S2c). However, perpendicular to the surface, the nearest Bi_3 atom relaxed downward, while a neighboring Cl_1 relaxed upward (Figure 1b and S2d). This different relaxation behavior, as characterized by the atoms moving along the open channel perpendicular to the (010) surface, was denoted as out-of-plane relaxation. Interestingly, different from the in-plane relaxation of Bi atoms around the OV on (001) surface, the out-of-plane relaxation happened on the (010) surface shortened the Bi_3-O_1 (or Bi_3-O_2) bond length from 2.39 Å to 2.33 Å, and the Bi_1-Cl_1 (or Bi_2-Cl_1) bond length from 2.93 Å to 2.82 Å. In order to experimentally characterize these different atom relaxation behaviors, we performed X-ray absorption fine structure (XAFS) spectroscopy, which is a powerful element-specific tool to study local atomic arrangements. Single crystalline BiOCl nanosheets exposed with (001) or (010) surface (denoted as BOC-001 or BOC-010) were prepared via a simple hydrothermal method (Figure S3). Their surface properties were characterized by zeta potential measurement and electrochemical impedance spectroscopy

(Figure S4). UV light illumination was used to create OVs on the surfaces to obtain their oxygen-deficient counterparts (denoted as BOC-001-OV or BOC-010-OV) (Figure S5). The Bi L-edge extended XAFS $k^2\chi(k)$ oscillation curves revealed that the formation of OVs did not significantly change the frequencies, but remarkably reduced the amplitude because of the surface distortion (Figure 1c). This could be further explicitly manifested by corresponding Fourier transform (FT) of the $k^2\chi(k)$ functions in R-space (Figure 1d). The FT curve of BOC-001 was characterized by two main peaks at 1.82 Å and 2.81 Å associated with the Bi-O and Bi-Cl coordination, respectively. For BOC-001 with OVs, the Bi-O peak position shifted to the higher R direction by 0.04 Å, while the Bi-Cl peak position remained unchanged (Figure 1d). To obtain quantitative structural parameters around the Bi atoms within BOC-001-OV, least-square curve parameter fitting of the Bi-O and Bi-Cl peaks was performed (Table S1). The coordination number for the surface interatomic Bi-O pair (N_{Bi-O}) decreased from 4.0 to 3.1, while the surface interatomic Bi-Cl pair (N_{Bi-Cl}) value slightly changed from 4.0 to 3.9, suggesting the generation of OVs rather than Cl vacancies on the (001) surface. Moreover, the increased surface Bi-O bond length corresponding to the high-R shift of Bi-O peak and the almost unchanged Bi-Cl bond length were consistent with the in-plane relaxation behavior of atoms around the OV of BiOCl (001) surface (Table S1). Similar with the case of BOC-001-OV, surface N_{Bi-O} of BOC-010-OV reduced from 3.7 to 2.8, while the N_{Bi-Cl} slightly decreased, indicating the presence of OVs. However, the peak positions of Bi-O and Bi-Cl of BOC-010-OV shifted to lower R direction by 0.07 Å and 0.09 Å, respectively. These shifts indicated the shortening of both Bi-O and Bi-Cl bond lengths, agreeing well with the out-of-plane relaxation behavior of atoms around the OV of (010) surface (Table S1).

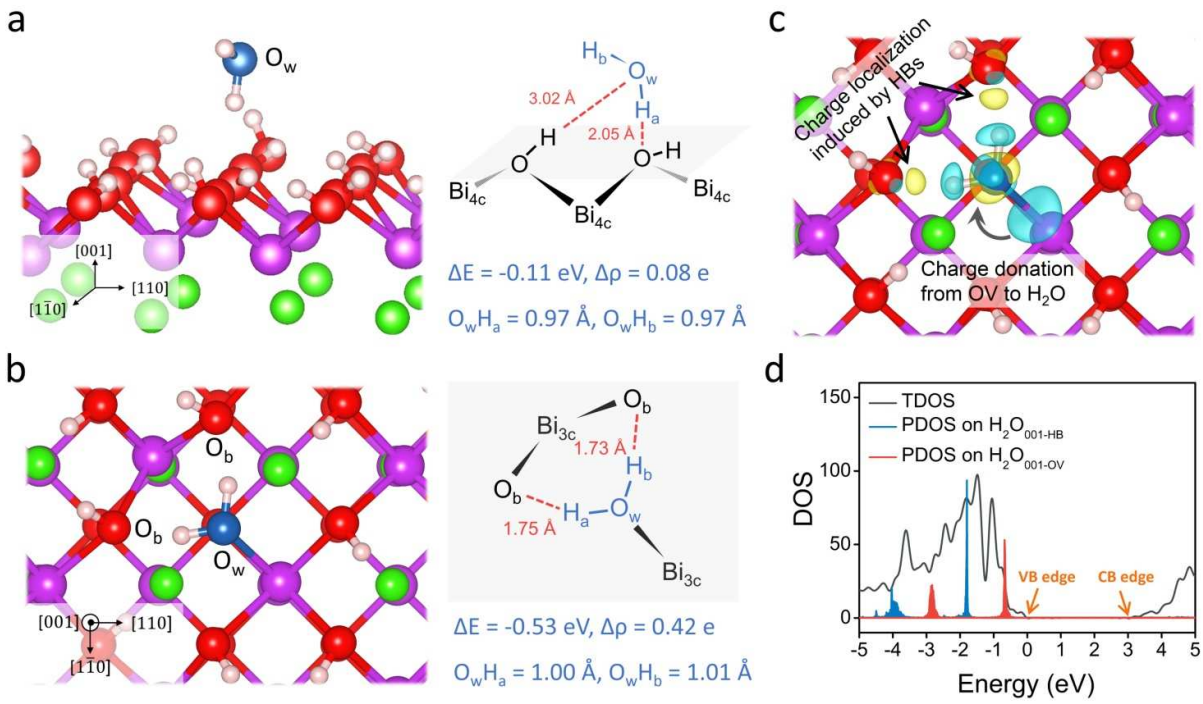

Figure 2. Theoretical study of water adsorption on the BiOCl (001) surface. (a) Adsorption of H_2O on defect-free BiOCl (001) surface. (b) Adsorption of H_2O on the BiOCl (001) surface with an OV and (c) the corresponding charge density difference. The yellow and blue isosurfaces represent charge accumulation and depletion in the space, respectively. For clarity, the symmetric parts of the optimized slabs at the bottom are not shown. The isovalue is 0.005 au. Red dashed lines in the schematic plots of the water adsorption structures show the ordinary HBs. ΔE is the water adsorption energy and the negative adsorption energy indicates the total energy decreases when water is adsorbed. Δρ is the Bader charge change of the adsorbed water. For clarity, the calculated Bader charge is the sum of Bader charge of three atoms of one water molecule and the positive values of Bader charge change mean the transfer of electrons from the BiOCl surface to the adsorbed H_2O. (d) The PDOS of water on (001) surface of BiOCl with different adsorption structures. For the sake of presentation, the local contributions have been scaled by a factor of ten.

Successful elucidation of the specific structures of OVs on the two prototypical BiOCl surfaces allowed us to testify our hypothesis whether OVs might serve as active sites for water activation toward enhanced thermodynamics of oxidation. On the defect-free BiOCl (001) surface, H_2O in the inner layer was mainly adsorbed via a hydrogen-bond (HB) network constructed by the interactions between hydroxyl groups of adsorbed H_2O and those on the surface (Figure 2a). The representative HB lengths (2.05 Å and 3.02 Å) were much longer than that (1.82 Å) of bulk water. This indicated the weak interaction between adsorbed H_2O with (001) surface, being further confirmed by the small adsorption energy of 0.11 eV and the absence of significant interfacial charge transfer according to Bader charge calculation (Figure 2a). Different from the isolated hydroxyl groups on many TiO_2 surfaces, hydroxyl groups on BiOCl (001) surface are rather immobile whose O atoms are strictly confined to the surface lattice that hinders their efficient three-dimensional relaxation. This difference might explain the weak interaction between water and the BiOCl (001) surface. After the introduction of an OV, H_2O was molecularly adsorbed at the OV site with its oxygen (O_w) roughly replacing the missing bridging oxygen and chemically bonding to a 3-coordinated Bi atom (Bi_{3c}) around the OV (Figure 2b). Compared with H_2O adsorbed on defect-free (001) surface via pure HBs, H_2O adsorbed on the OV was more exothermic by 0.42 eV. Interestingly, the molecular plane of H_2O, which was initially perpendicular to the (001) surface, performed reorientation around its figure axis with the most stable orientation being parallel to the surface, as two relatively strong HBs (1.75 Å and 1.73 Å) were formed between the $-O_wH_a$ ($-O_wH_b$) group of adsorbed H_2O and adjacent bridging O atom (O_b) (Figure 2b). We then adopted charge density difference to trace the origin of these two HBs, and first found a distinct charge donation from OV to the adsorbed H_2O, as characterized by the depletion of electrons localized on the Bi_{3c} near the OV and the accumulation of

electrons on O_w (Figure 2c). Meanwhile, the accumulation of electrons on O_w enhanced the hydrogen-donor nature of -O_wH, and the appearance of charge localization in the region between -O_wH_a (-O_wH_b) and O_b provided a clear picture of these two HBs' formation process (Figure 2c).[28] Bader charge calculation revealed a net charge transfer of 0.42 e from the defective BiOCl (001) surface to the adsorbed H_2O, making the adsorbed H_2O negatively charged. To estimate the energetics of H_2O with different adsorption modes to trap photogenerated holes, we examined the partial density of states (PDOS) of the adsorbed H_2O. PDOS of H_2O bound to the defect-free (001) surface via HB interaction ($H_2O_{001\text{-}HB}$) was embedded in the VB, approximately 1.76 eV more negative than the VB edge (also VB maximum) (Figure 2d). However, after the introduction of an OV, PDOS of OV-adsorbed H_2O ($H_2O_{001\text{-}OV}$) was shifted to the VB edge by 1.07 eV. This shift narrowed the distance between PDOS of adsorbed H_2O and the VB edge from 1.76 eV to 0.69 eV. We therefore proposed that OVs on BOC-001 surface could provide the new sites to enhance the water adsorption, and also activate the adsorbed water, enhancing the hole trapping by the adsorbed water thermodynamically.

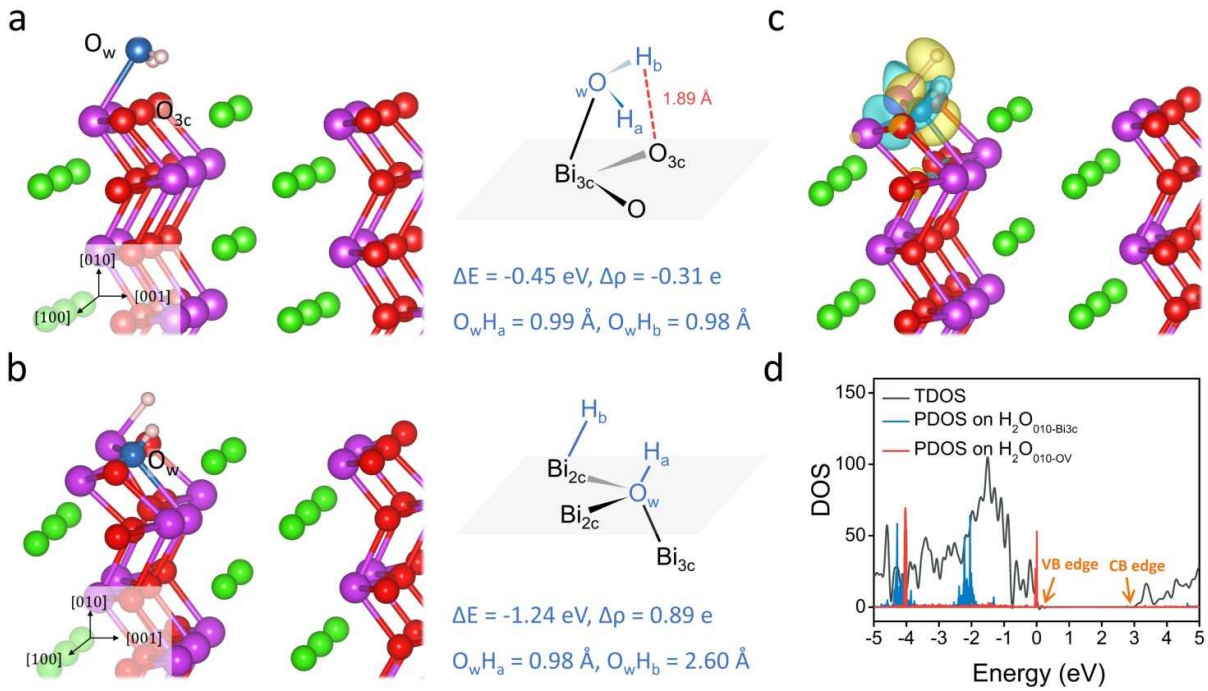

Figure 3. Theoretical study of water adsorption on the BiOCl (010) surface. (a) Adsorption of H_2O on the defect-free BiOCl (010) surface. (b) Adsorption of H_2O on the BiOCl (010) surface with an OV and (c) the corresponding charge density difference. (d) The PDOS of H_2O on the (010) surface of BiOCl with different adsorption structures. For the sake of presentation, the local contributions have been scaled by a factor of ten.

As for the defect-free (010) surface of BiOCl, both Bi and O atoms of unsaturated coordination are supposed to act as reliable Lewis acid and base sites for the inner layer water adsorption.[29-32] Within expectation, H_2O was adsorbed molecularly with the O_w chemically bound to a (010) surface 3-coordinated Bi atom (Bi_{3c}), which was 0.34 eV more exothermic than the H_2O adsorption on the perfect (001) surface (Figure 3a). Meanwhile, H_2O exhibited reorientation with the molecular plane being almost parallel to the (010) surface because of the HB interaction between -OH_b of H_2O and a surface 3-coordinated O atom (O_{3c}) with a moderate HB of 1.89 Å (Figure 3a). The formation of this HB via sharing the H_b atom of adsorbed H_2O to electron donors of O_{3c} slightly elongated the O-H_b

bond to 0.99 Å (Figure 3a). Similar with previous reports over H_2O adsorption on 5-coordinated Ti of TiO_2 surfaces, these Lewis acid-base interactions remarkably decreased the electron density on adsorbed H_2O, as reflected by a net charge transfer of 0.31 e from the adsorbed H_2O to BiOCl (010) surface according to the Bader charge calculation. After the generation of an OV on the (010) surface, the Bi_{3c}-bound H_2O would diffuse to the OV, where spontaneous dissociation took place with the $-O_wH_a$ group being pinned at the OV and the proton fragment $-H_b$ being transferred to a 2-fold coordination unsaturated Bi atoms (Bi_{2c}) around the OV (Figure 3b). Apparently, H_2O on the OV of BiOCl (010) surface preferred to dissociate in comparison with that of (001) surface, which might be explained as follows. First, the water dissociation on the OVs of oxide surfaces is highly related to the sufficient charge transfer from the OV to the adsorbed water. This is because the O-H bonds of water will not break without sufficient interfacial charge transfer.[33-36] As expected, isodensity contour plot of the corresponding charge density difference of H_2O adsorbed on the OV of BiOCl (010) surface, being characterized by the significant charge depletion on Bi_{2c} atoms around the OV along with the charge accumulation on the dissociated $-O_wH_a$ and $-H_b$ fragments, suggested that the donation of electrons from the OV of (010) surface to H_2O was definitely more favorable than that on the defective (001) surface (Figure 3c). Consistently, Bader charge change (0.89 e) of dissociatively adsorbed H_2O was much more than that (0.42 e) of the molecularly adsorbed one, confirming the OV on the BiOCl (010) surface allowed more electrons donated to the dissociatively adsorbed H_2O. Second, the water dissociation on the OV requires an available site to accept the dissociated -H fragment for the well stabilization of dissociated state.[37-39] On the OV of BiOCl (001) surface, even though adsorbed H_2O could form strong HBs with bridging O atoms that significantly elongated the $O\text{-}H_a$ (or $O\text{-}H_b$) bond from 0.97 to 1.00 Å, spontaneous dissociation was still

prohibited because each bridging O atom had already been bound to a proton, impeding its acceptance of another proton because of steric hindrance (Figure 2b).[40] As for the OV of BiOCl (010) surface, Bi_{2c} atom near the OV provided the suitable site to bind the -H_a fragment. We have to point out here that the binding of dissociated -H_b fragment to surface Bi_{2c} atom is actually an unusual water dissociation mode because the expected site for the dissociated proton transfer is the surface O_{3c} atom toward the formation of another -OH_b group. This unexpected binding behavior is believed to be a thermodynamic requirement for the surface energy minimization. Our previous work revealed that the introduction of OVs on the BiOCl surface typically produced new states in the bandgap, which were fully occupied with electrons along with the formation of dangling bonds on the two Bi_{2c} atoms near the OVs, making the defective surface highly unstable.[26] Similar dangling bonds on the coordination unsaturated cations were found on the Ta_3N_5 (100) surface with nitrogen vacancies, the Si terminated SiC (001) surface and the FeO (111) surface with OVs, all of which can be effectively stabilized by the dissociative water adsorption with the -H fragment being bound to these unsaturated cations.[35, 41, 42] The corresponding H_2O adsorption energy of -1.24 eV on the OV of BiOCl (010) surface, which was much more exothermic than that (-0.53 eV) of defective (001) surface, confirmed the (010) surface with an OV was greatly stabilized by this kind of dissociative water adsorption behavior. PDOS of molecularly adsorbed H_2O on the BiOCl (010) surface via Lewis acid-base interactions ($H_2O_{010\text{-}Bi3c}$) accompanied by the charge transfer from H_2O to (010) surface was deeply embedded in VB by about 2.07 eV (Figure 3d). However, the introduction of an OV, which reversed the interfacial charge flow direction, remarkably upshifted the PDOS of dissociatively adsorbed H_2O ($H_2O_{010\text{-}OV}$) to almost overlap the VB edge of BiOCl. This remarkable

change suggested the water activation towards oxidation on the OV of BiOCl (010) surface might be more favorable than that on the defective (001) surface (Figure 3d).

Although the above theoretical calculations revealed that both the (001) and (010) surfaces of BiOCl could realize water activation after the OV introduction, it remained unknown which adsorption mode (molecular or dissociative) more favored the photocatalytic water oxidation, considering that both the adsorption and electronic structures of OV-adsorbed H_2O were different on various BiOCl surfaces. To answer this question, we would like to focus on the first proton removal reaction ($H_2O^* + hole^+ \rightarrow \bullet OH^* + H^+$), which is considered as the key kinetic step of water oxidation.[5-7] As aforementioned, this reaction involves two elementary steps, the O-H bond breaking step that is typically regarded as a surface-catalyzed process dependent on the surface local bonding geometry, and the hole trapping step that is a light-driving process related to the electronic state of adsorbed water.[6,7] We thus assumed the oxidation of dissociatively adsorbed H_2O on the OV of BiOCl (010) surface was more favorable than the molecular adsorbed one on the OV of (001) surface because of the following two reasons. First, the O-H bond breaking on the OV of BiOCl (010) surface was a barrierless process for the dissociative H_2O adsorption. However, as for the molecular adsorption of H_2O on the OV of (001) surface, it was merely an activated process and extra energy was then required to break one of the O-H bonds. Second, compared with the PDOS of molecularly adsorbed H_2O on the OV of BiOCl (001) surface with a distance of 0.69 eV to the VB edge, PDOS of dissociatively adsorbed H_2O on the OV of (010) surface almost overlapped with the VB edge, suggesting its higher activation level and higher tendency to trap holes (Figure 2d and 3d). The donation of electrons from the OV to the adsorbed water was undoubtedly responsible for the water activation as we discussed above, while the activation level was highly dependent on the

amount of donated electrons. Bader charge calculations revealed that the dissociatively adsorbed H_2O accepted more electrons than the molecularly adsorbed H_2O on the OV of BiOCl surfaces, which was basically consistent with the fact that dissociated hydroxyl was a better electron acceptor than molecular water.[13] Therefore, we believe that OVs on BiOCl surface offer a possibility to energize the sluggish water oxidation through water activation, while the activation states related to both the geometrical and electronic structure of adsorbed H_2O are highly dependent on the structures of OVs.

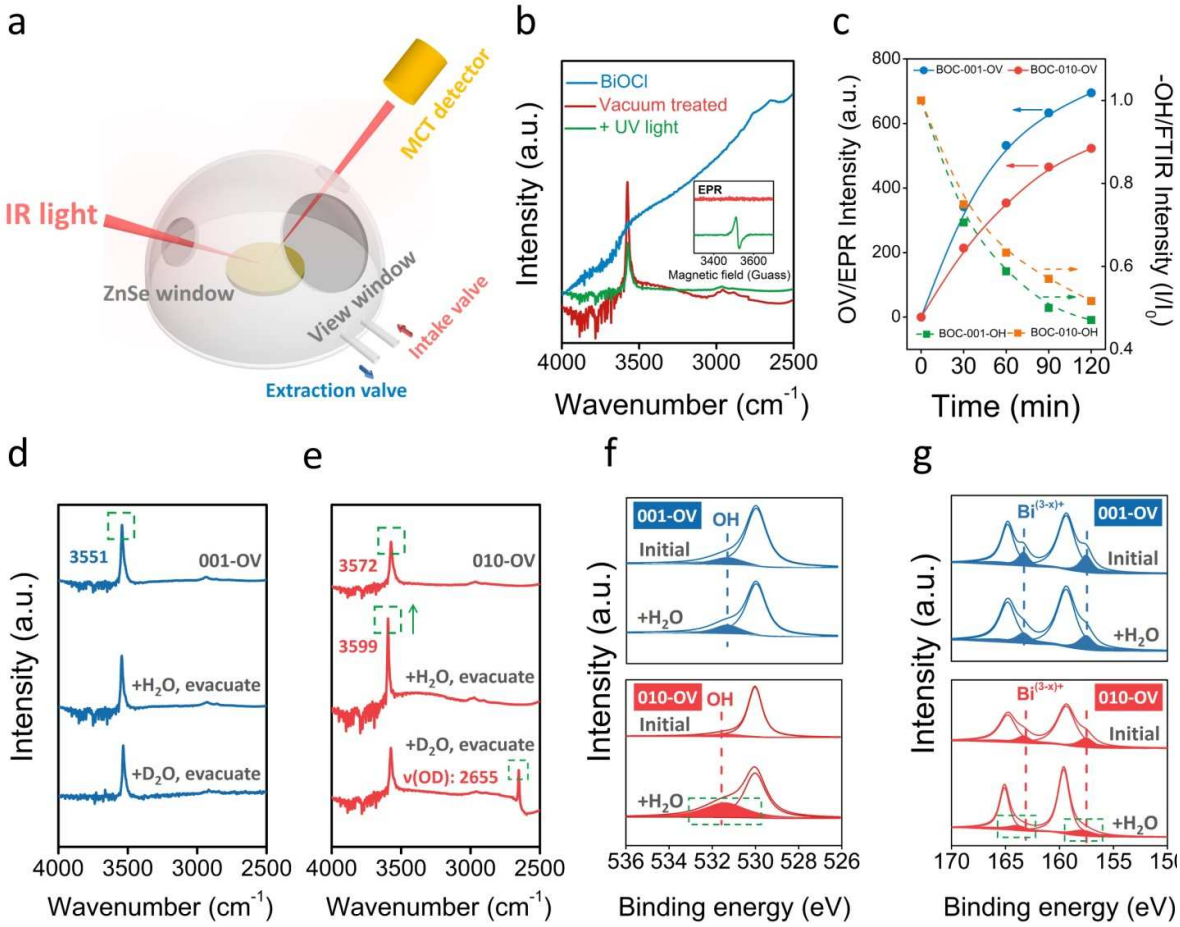

Figure 4. Experimental study of the water adsorption on the BiOCl surfaces. (a) Designed reaction cell for the FTIR signal recording. BiOCl samples, after being pressed into cylindrical pellets, were put in the center of the reaction cell. The cover dome was equipped with three windows. Two of the

windows were made of ZnSe and permitted entry and exit of the detection infrared beam, whereas the third (quartz) view window was for the observation as well as the transmission of a UV light. The IR signal was *in situ* collected through a HgCdTe (MCT) detector along with the photoreactions. (b) Representative FTIR spectra of the pristine, vacuum-treated and subsequent UV-illuminated BiOCl surfaces and the typical low-temperature EPR signal corresponding to *in situ*-created OVs (inset). (c) Dynamic change of the OV EPR signal intensity (solid lines) and normalized -OH FTIR signal intensity (dashed lines) of the BiOCl (001) and (010) surface along with the UV light illumination. Recording of the surface FTIR spectra under certain reaction conditions over BOC-001-OV (d) and BOC-010-OV (e). High resolution of the O1s (f) and Bi4f (g) spectra of the BiOCl surfaces containing OVs before and after exposure to water vapor.

To verify these theoretical calculation results of the OV-structure-dependent water activation, it is first necessary to experimentally determine the different water adsorption structures, which is extremely challenging especially for the study of dissociative adsorption mode. Common methods to characterize the water adsorption structure on oxide surface are based on scanning tunneling microscope and temperature-programmed desorption.[30,34,39,43,44] In this study, we for the first time adopted FTIR spectroscopy to study the water adsorption behavior. Since surface hydroxyl groups are often interfered by the trace amount of adsorbed water via their strong interactions, FTIR is used to work in tandem with vacuum surface science in a designed reaction cell equipped with facilities for sample heating, cooling and for the reaction atmosphere controlling (Figure 4a). The FTIR spectra of untreated BiOCl (BOC-001 or BOC-010) displayed a rising and broad band spanning 3250-3750 cm^{-1} arisen from the water hydrogen-bonded hydroxyl stretching (Figure 4b). However, after the thermal treatment (120 min at 380 K) under high vacuum (~10^{-6} mbar) to remove most of

the initially surface-adsorbed molecular water, this feature largely disappeared, accompanying with the appearance of a discrete and narrow vibration around 3500 cm^{-1} corresponding to the surface hydroxyl groups (Figure 4b). When the whole reaction cell was cooled to room temperature, a UV light (λ = 254 nm) was then applied to shine the sample through the quartz view window to *in situ* create OVs on the BiOCl surfaces. After irradiation, both BOC-001 and BOC-010 exhibited a typical OV signal according to the low temperature electron paramagnetic resonance (EPR) spectra (inset of Figure 4b). Meanwhile, the amount of surface hydroxyl groups (dashed lines) over BOC-001 and BOC-010 gradually decreased along with the OVs' concentration increase (solid lines) (Figure 4c). After the *in situ* formation of OVs, water-saturated Ar gas was then introduced to the reaction cell to maximize adsorption of water onto the BiOCl surfaces. After a sufficient static reaction between the adsorbed water and OVs of BiOCl in the dark, the reaction cell was re-evacuated via thermal and vacuum treatment. This treatment was supposed to desorb the subsequently-pumped gaseous water, but left behind the possible newly-formed surface hydroxyl groups arisen from water dissociation at the OVs, which allowed the direct visualization of the hydroxyl groups' change. After the reaction between OVs and H_2O, both the intensity and the position of surface hydroxyl absorption band on BOC-001-OV exhibited no obvious change, but the absorption band intensity was significantly enhanced in the case of BOC-010-OV (Figure 4d and 4e). This difference suggested that water was molecularly adsorbed on the OVs of BOC-001, which could be easily removed by the thermal and vacuum treatment, but irreversibly dissociated on the OVs of BOC-010 to generate new hydroxyls covering OVs, resulting in the increase of overall surface hydroxyls density. Moreover, the band position of surface hydroxyls on BOC-010-OV slightly shifted from 3572 cm^{-1} to a higher wavenumber of 3599 cm^{-1} (Figure 4d). This shift was attributed to the increased electron density on

the O_w atom caused by charge transfer from the OV of BiOCl (010) surface to newly-formed dissociated -O_wH_a fragment, leading to a higher O_w-H_a vibrational frequency (Figure 3b and 3c).[45] When D_2O vapor was used instead of H_2O vapor, new absorption band corresponded to the -OD stretching emerged at 2655 cm^{-1} on BOC-010-OV, which was stably observed up to 550 K (Figure 4e). This clearly demonstrated the dissociative adsorption of D_2O on the OVs of BiOCl (010) surface. The increased density of surface hydroxyl groups arisen from the water dissociation on the OVs of BOC-010 was also confirmed by the X-ray photoelectron spectroscopy (XPS). The O1s spectra of BOC-001-OV showed a broader shoulder with a chemical shift of 1.5 eV relative to the oxide O 1s peak, being attributed to surface hydroxyl groups. After the water vapor exposure, the intensity of this shoulder changed slightly, but was remarkably enhanced in the case of BOC-010-OV (Figure 4f). This enhancement corresponded to the increase of surface hydroxyl groups originated from the water dissociation on OVs of BiOCl (010) surface. Along with the water dissociation, we also observed the electronic states change associated with the OVs oxidation of BOC-010. Bi4f spectra of the BOC-010-OV showed two additional shoulder peaks at 163.3 and 157.5 eV of lower binding energies, which were corresponded the reduced Bi states of $Bi^{(3-x)+}$ around the OVs (Figure 4g). After exposure to water vapor, these shoulder peaks on BOC-010-OV were largely depopulated, which were slightly attenuated in the case of BOC-001-OV (Figure 4g). Depopulation of the defect states in the Bi 4f spectra, reflecting a decreased concentration of OVs, supported our DFT calculation results that interaction of water with the OV of BiOCl (010) surface involved the simple adsorption, and also the surface redox reaction, where $Bi^{(3-x)+}$ were reoxidized by the adsorbed water via the charge donation from OVs to the newly-formed hydroxyl groups (Figure 3c).

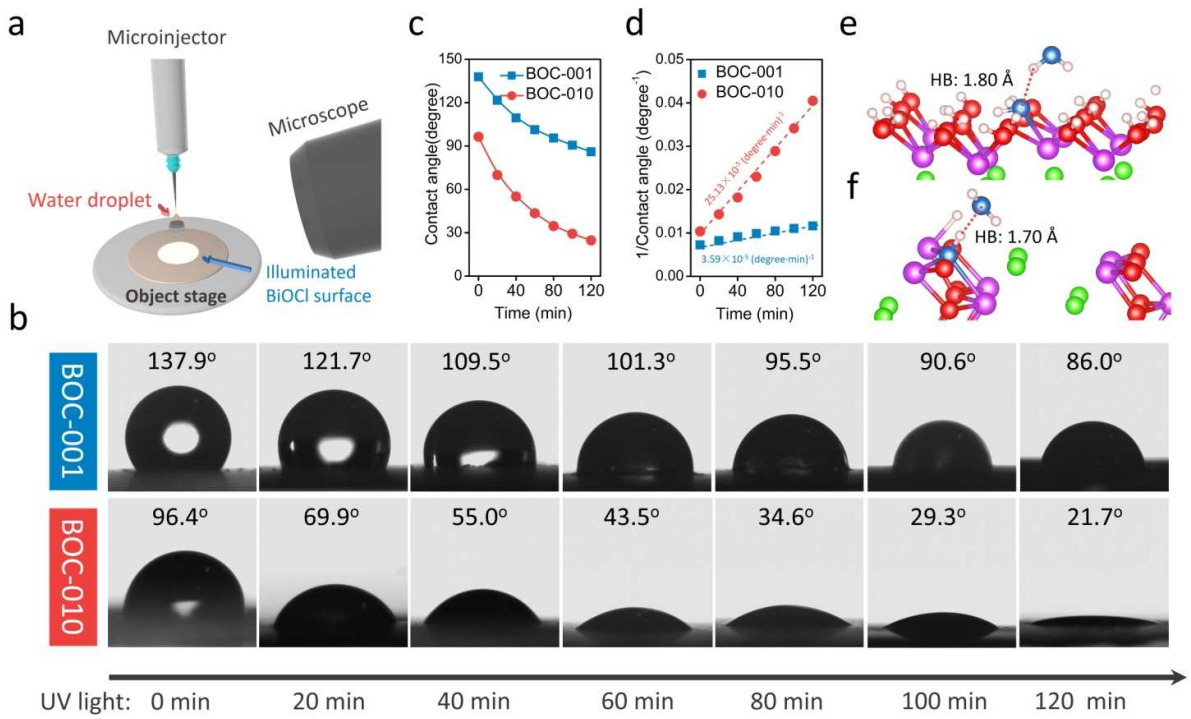

Figure 5. *In situ* water contact angle measurements on the BiOCl surfaces. (a) Schematic presentation of water contact angle measurement. A UV light source was set above the BiOCl cylindrical pellets and water contact angle was *in situ* monitored via a microscope connected to a computer. (b) Photos of the water droplets on the BiOCl surfaces under UV light illumination. The final contact angle was an average of six measurements on the different locations on the surfaces. (c) Dynamic change of the water contact angles and (d) water contact angle reciprocals on the BiOCl surfaces along with UV light illumination. Theoretical simulation of water adsorption structures in the outer layer on the (e) BOC-001 and (d) BOC-010 with an OV.

Enlightened by the above FTIR and XPS results, we further evidenced the different microscopic water-surface interaction modes via the macroscopic water adsorption on the BiOCl surfaces monitored by the *in situ* water contact angle measurements (Figure 5a). Defect-free BOC-001 was rather hydrophobic with an initial water contact angle of 137.9°, confirming the weak interaction between water and this surface. Under UV light irradiation for 120 min, the water contact angle on

BOC-001 gradually decreased to 86°, indicative of slight hydrophilic character (Figure 5b). As compared with BOC-001, BOC-010 showed a quite different water wetting behavior. First, initial water contact angle on BOC-010 was around 96.4°, significantly smaller than that on BOC-001, indicating the stronger interaction between water molecules and BOC-010. Second, the water contact angle on BOC-010 surface quickly decreased to 21.7° within 120 min of UV light illumination, showing a more rapid conversion from hydrophobicity to hydrophilicity (Figure 5b). For comparison, dark control experiments were performed, which revealed that the water contact angles did not change along with time in the dark (Figure S6). Photoinduced hydrophilic conversion on both the BiOCl surfaces could be undoubtedly related to the presence of OVs, as the hydrophilic surface did not appear when control experiments were conducted in the O_2 atmosphere to quickly quench the *in situ*-formed OVs.[46-50] Plotting the water contact angle against UV light illumination gave trends of the surface hydrophilicity evolution, but could not provide specific kinetic information on the surface hydrophilicity change because the initial values of water contact angles on BiOCl surfaces were different (Figure 5c). So we plotted the reciprocal of the contact angle against the UV light irradiation time, which gave nearly straight lines whose corresponding slopes could be defined as the hydrophilic conversion rates (k_h) (Figure 5d).[46] The estimated k_h values of BOC-001 and BOC-010 were 3.59×10^{-5} and 25.13×10^{-5} (degree • min)$^{-1}$, respectively. Therefore, the photoinduced hydrophilic conversion rate of BOC-010 was about 7 times that of BOC-001. The photoinduced hydrophilic conversion rate difference between BOC-001 and BOC-010 under the same conditions was actually attributed to their different interaction strengths between the inner layer water and the outer layer water. Molecular water adsorption on the OV of BiOCl (001) surface in the inner layer made O_w of the adsorbed water a credible HB acceptor site for the enhanced outer

layer water adsorption with a moderate HB bond of 1.80 Å (Figure 5e). However, in the case of BiOCl (010) surface, water dissociation along with the charge transfer from OV to water offered the dissociated -O_wH_a fragment a perfect HB donor site toward the formation of an intimately surface-bound OH-H_2O complex with a much stronger HB of 1.70 Å (Figure 5f). Therefore, both the higher binding energy for water adsorption in the inner layer and the stronger HB water formed in the outer layer determined the hydrophilicity character of BOC-010 under UV light.

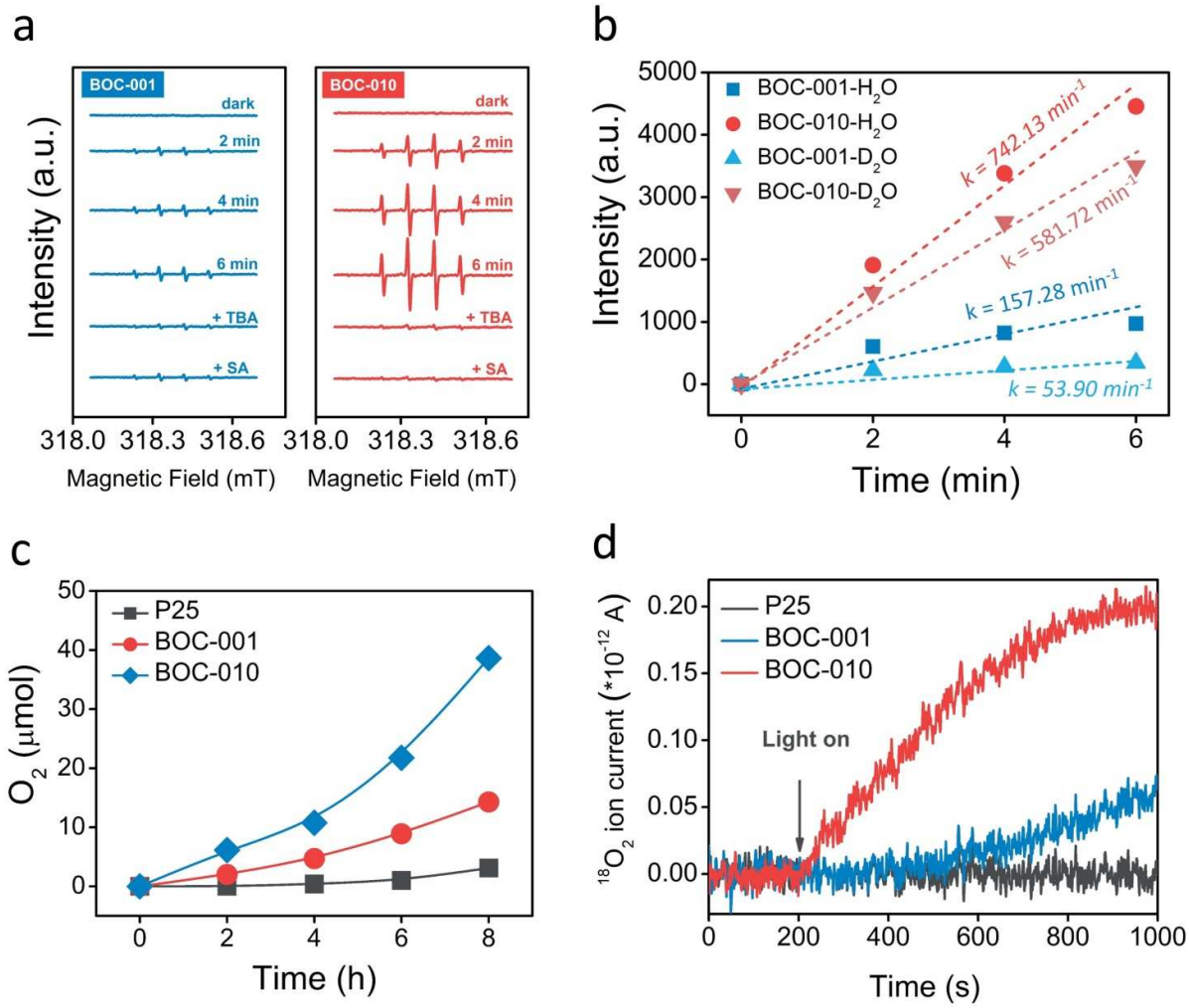

Figure 6. Experimental study of water oxidation on the BiOCl surfaces. (a) EPR spectra of the spin-reactive •OH radicals photogenerated by BiOCl in H_2O. (b) Qualitative determination of the •OH radicals in H_2O or D_2O photogenerated by BiOCl along with UV light illumination. (c) O_2

evolution upon UV light irradiation over BiOCl in H_2O. (d) Time course for the generation of $^{18}O_2$ from $H_2{}^{18}O$ by BiOCl detected via mass spectra.

The above results and discussions provided the solid evidences that water molecules were molecularly adsorbed on the OVs of BiOCl (001) surface, but dissociatively adsorbed on the OVs of BiOCl (010) surface. However, we still needed check our speculation whether the dissociatively adsorbed water molecules with more suitable geometrical structure and higher-level of activation would indeed exhibit higher tendency toward oxidation than the molecularly adsorbed ones. To answer this question, EPR was first used to determine the primary photocatalytic water oxidation active species of •OH radicals either adsorbed on BiOCl surfaces or dissolved in the water solution, which were generated via the first proton removal reaction ($H_2O^* + hole^+ \rightarrow \bullet OH^* + H^+$). To exclude the possibility of •OH radicals formation via the O_2 reduction pathway, Ar was continuously purged to completely remove the water-dissolved O_2. No EPR signal could be observed in the dark. As expected, we observed strong four-line EPR spectra with the relative intensities of 1:2:2:1 corresponding to •OH radicals for both BOC-001 and BOC-010 under UV light irradiation (Figure 6a). These EPR signals could be largely inhibited by adding either *tert*-butyl alcohol (TBA) or sodium acetate (SA) as the •OH radicals or holes scavenger, indicating the generation of •OH radicals was directly related to water oxidation by photogenerated holes (Figure 6a). Plotting the intensity of the EPR signal intensity against the irradiation time gave nearly two straight lines, whose slopes indirectly gave the •OH radicals' generation rates and were estimated to be 157.28 and 742.13 min^{-1} for BOC-001 and BOC-010, respectively (Figure 6b). Therefore, the water oxidation on BOC-010 toward the formation of •OH radicals was about 4.7 times that on BOC-001. This higher photoreactivity of BOC-010 was not attributed to its specific surface area, which was only 2.8

times that of BOC-001 (Figure S4c). Meanwhile, when D_2O was used instead of H_2O, BOC-001 showed a deuterium kinetic isotope effect (KIE = k_{H2O}/k_{D2O}) of 2.92, a characteristic value indicating breakage of the O-H bond is the rate-limiting step of the first proton removal reaction.[5-7] However, as for BOC-010, whose *in situ* formed OVs could directly catalyze the O-H bond breaking prior to oxidation due to water dissociation, showed a much smaller KIE of 1.28 (Figure 6b). We also qualitatively measured the amount of free •OH radicals as well as their coupling product of H_2O_2 via photoluminescence. In accordance with the EPR results, BOC-010 possessed much faster reactive oxygen species generation rate than BOC-001 (Figure S7b and S7c). Moreover, the higher concentration of •OH and H_2O_2 generated by BOC-010 surface endowed its higher photoreactivity than BOC-001 for the anaerobic removal of pentachlorophenol with good recyclability and stability (Figure S7d-f and S8). The multihole water oxidation products of O_2 over the BiOCl surfaces were also investigated. Although the adsorption of O_2 was more preferential than that of H_2O on the OV of BiOCl surfaces (Figure S9), as compared with TiO_2-P25 which cannot *in situ* generate OVs under UV light, BiOCl still exhibited remarkable capability to oxidize water into O_2 (Figure 6c). Since no electron scavenger was added during O_2 evolution reaction, these results clearly demonstrated the indispensable role of the *in situ* formed OVs on the BiOCl surfaces toward enhanced thermodynamics for water oxidation, while the higher photoreactivity of BOC-010 was attributed to the higher-level activation of dissociatively adsorbed H_2O. In order to exclude the possible interference of $^{16}O_2$ in air, water oxidation with BiOCl photocatalysts were also carried in $H_2{}^{18}O$ under UV light. Photogenerated $^{18}O_2$ was detected by mass spectrometry and the signal for $^{18}O_2$ (m/z =36) gradually increased for the BiOCl catalysts, while was not detected in case of P25 (Figure 6d). The much higher signal intensity for $^{18}O_2$ of BOC-010 confirmed its higher photoreactivity toward

water oxidation than that of BOC-001. Because only traces of H_2 was detected, the twinborn photoinduced electrons might be either scavenged by some of the surface-adsorbed O_2 for the OVs quenching, being reflected by equilibrium over the generation and consumption of OVs, and/or migrated into the aqueous solution to became solvated electrons (Figure S10).[24,51] Similar water activation scheme could also be observed over BiOBr and BiOI, the homologous photocatalysts of BiOCl. Both stoichiometric BiOBr and BiOI could not oxidize water to generate •OH radicals under visible light, but after the introduction of OVs on the catalysts surface, distinct EPR signals correspond to •OH radicals were promptly observed, indicating the indispensable role of OVs for water activation (Figure S11).

Conclusions

In summary, DFT calculations together with XAFS spectroscopy were first adopted to determine the specific structures of OVs on the (001) and (010) surfaces of BiOCl. Further theoretical and experimental results demonstrated OVs could activate adsorbed water via their localized electrons, offering a possibility to enhance the thermodynamics toward water oxidation, while the water activation state was supposed to be highly dependent on the structures of OVs. In our case, the OVs of BiOCl (010) surface with dissociatively adsorbed water exhibited much higher photoreactivity toward oxidation than those of BiOCl (010) surface with the molecularly adsorbed water, generating more water-oxidized species like •OH, H_2O_2 and O_2. It was proposed that OVs of BiOCl (010) surface could facilitate the barrierless O-H bond breaking of the first proton removal reaction, which was sterically hindered on the OVs of BiOCl (001) surface, and also allow more electron transfer from the OVs to dissociatively adsorbed water, leading to a higher water activation level. These

findings highlight the indispensable role of crystalline surface structure on water oxidation, and may open up new avenues for the rational design of new photocatalysts via surface engineering.

Experimental Section

Chemicals. All chemicals used were purchased from Sinopharm Chemical Reagent Co., Ltd. (Shanghai, China) and were of analytical grade and used without purification.

Preparation of BiOCl single-crystalline nanosheets. Well-defined BiOCl single-crystalline nanosheets were prepared by our previous method.[52] Typically, $Bi(NO_3)_3 \cdot 5H_2O$ was added into 18 mL distilled water with stoichiometric amount of KCl. The solution with pH adjusted be either 1 or 6 was then poured into an autoclave and was heated at 220 °C for 24 h. Resulting precipitates were washed with deionized water and ethanol for 6 times and dried at 80 °C for 24 h in air. We denoted the BiOCl nanosheets obtained under pH = 1 with (001) surface exposed as BOC-001 and the BiOCl nanosheets obtained under pH = 6 with (010) surface exposed as BOC-010. 0.2 g BOC-001 or BOC-010 was then immersed into 50 mL distilled water and illuminated with a UV light (λ = 254 nm, 30 W) under continuous Ar purging for 4 h to obtain its oxygen-deficient counterpart BOC-001-OV or BOC-010-OV.

Characterization. *In situ* diffuse reflectance FTIR spectra were recorded by Nicolet iS50FT-IR spectrometer. XPS was obtained with Perkin-Elmer PHI 5000C and all binding energies were calibrated by using the contaminant carbon (C1S = 284.6 eV) as a reference. Water contact angles of BiOCl surfaces were measured by a sessile drop method at room temperature with a contact angle goniometer (OCA-20, DataPhysics, Germany) equipped with video capture. For every measurement, 2 μL of deionized water droplet was used. Electron paramagnetic resonance (EPR) spectra were conducted on a Bruker EMX EPR Spectrometer (Billerica, MA). Bismuth L-edge extended X-ray absorption fine structure (EXAFS) spectra were performed at the beamline 1W1B of Beijing Synchrotron Radiation Facility, Institute of High Energy Physics, Chinese Academy of Sciences.

The electron energy in the storage ring was about 2.2 GeV with a current of about 100 mA. Incident X-ray energy was scanned across the EXAFS region of the Bi L-edge (13426 eV) using a Si (111) double crystal monochromator. The EXAFS data were converted to R-space by taking the Fourier transform of $\chi(k)$ function. Fitting was performed simultaneously on all data sets in R-space using the program Artemis to optimize the coordination number (N), the distance (R), and disorder (σ^2).

DFT theoretical calculation. All the above calculations were performed using the first-principles density of functional theory (DFT) + *U* calculations with the exchange-correlation energy functional, which were described by generalized gradient approximation with Perdew-Burke-Ernzerhof (PBE) exchange-correlation function.[53] In order to test the thickness of the atomic layers of the slabs for all the BiOCl models, (1 × 1) surface was applied and this part of calculations were implemented by the CASTEP code in which plane-wave pseudopotential approach and ultrasoft pseudopotentials were employed for all the atoms with a kinetic energy cutoff of 380 eV.[54,55] All the structures were relaxed to an energy convergence of 10^{-5} eV/atom and a force convergence of 0.03 eV/Å during the geometrical optimization process. The Monkhorst-Pack mesh for BiOCl (001) and (010) surfaces were 4 × 4 × 1 and 2 × 4 × 1, respectively.[56] To simulate the water adsorption on the BiOCl surfaces, a (2 × 2) surpercell was used and enabled by a VASP code in which the projector augmented wave (PAW) method represented the electron-ion interaction with a kinetic energy cutoff of 520 eV.[57, 58] The energy and force converged to 10^{-5} eV/atom and 0.02 eV/Å during the geometrical optimization, respectively. In the energy and DOS calculation parts, the k-points were increased to 4×4×1 and 3×6×1 for the (001) and (010) surface, respectively. The vacuum in all the models was kept at 20 Å. The interaction energy of the adsorbate water on BiOCl surface was calculated as: $\Delta E = E(BiOCl + H_2O) - E(BiOCl) - E(H_2O)$. The charge density difference was calculated as: $\Delta\rho = \rho(H_2O/BiOCl) -$

$\rho(H_2O)$ -$\rho(BiOCl)$, where $\rho(H_2O/BiOCl)$ is the density of the interacting water-surface system, whereas $\rho(H_2O)$ and $\rho(BiOCl)$ are the densities of the two isolated (noninteracting) subsystems, taken in the same geometry of the interacting system. The desorption energy of O_2-adsorbed BiOCl surface was calculated as: $\Delta E = E(BiOCl) + E(O_2) - E(BiOCl + O_2)$.

Photocatalytic water oxidation. All photocatalytic water oxidation experiments were conducted at ambient temperature using a UV light (λ = 254 nm, 30 W) or a 500 W Xe arc lamp with a 420 nm cutoff filter as the visible light source. The photogenerated •OH radicals were detected via EPR using 5,5-dimethyl-1-pyrroline-N-oxide as the radical spin-trapped reagent. For photocatalytic oxygen evolution, 0.2 g photocatalyst was added into 100 mL of H_2O in a Pyrex flask reactor sealed with a silicone rubber septum. The reactor was also surrounded with water circulation in the outer jacket in order to maintain at room temperature. The mixture was continuously stirred in the dark with high-purity Ar bubbled to completely remove the dissolved O_2 for 120 min. Isotopic study was performed by mixing 0.02 g BiOCl mixed with 1 mL of $H_2{}^{18}O$ in a sealed Pyrex vessel. Generated $^{18}O_2$ during the photocatalytic water oxidation was monitored by a mass spectrometer (Trace 1300-ISQ, Thermo).

Supporting Information. Other experimental details, additional SEM and TEM images, X-ray diffraction patterns (XRD) and additional data. This material is available free of charge via the Internet at http://pubs.acs.org.

ACKNOWLEDGMENT

This work was supported by National Natural Science Funds for Distinguished Young Scholars (Grant 21425728), National Basic Research Program of China (973 Program) (Grant

2013CB632402), National Key Research and Development Program of China (Grant 2016YFA0203002), National Science Foundation of China (Grant 51472100), Self-Determined Research Funds of CCNU from the Colleges' Basic Research and Operation of MOE (Grant CCNU14Z01001 and CCNU16A02029), Excellent Doctorial Dissertation Cultivation Grant from Central China Normal University (Grant 2015YBZD018 and 2016YBZZ034). We also thank the National Supercomputer Center in Jinan for providing high performance computation.

REFERENCES

(1) Hoffmann, M. R.; Martin, S. T.; Choi, W.; Bahnemann, D. W. *Chem. Rev.* **1995**, *95*, 69–96.

(2) Ma, Y.; Wang, X.; Jia, Y.; Chen, X.; Han, H.; Li, C. *Chem. Rev.* **2014**, *114*, 9987–10043.

(3) Bourikas, K.; Kordulis, C.; Lycourghiotis, A. *Chem. Rev.* **2014**, *114*, 9754–9823.

(4) Kumar, S.; Schelling, P. K. *J. Chem. Phys.* **2006**, *125*, 204704.

(5) Valdés, A.; Kroes, G.-J. *J. Phys. Chem. C* **2010**, *114*, 1701–1708.

(6) Zhao, W.-N.; Liu, Z.-P. *Chem. Sci.* **2014**, *5*, 2256–2264.

(7) Chen, J.; Li, Y.-F.; Sit, P.; Selloni, A. *J. Am. Chem. Soc.* **2013**, *135*, 18774–18777.

(8) Youngblood, W. J.; Lee, S.-H. A.; Maeda, K.; Mallouk, T. E. *Acc. Chem. Res.* **2009**, *42*, 1966–1973.

(9) Qu, Y.; Duan, X. *Chem. Soc. Rev.* **2013**, *42*, 2568–2580.

(10) Li, H.; Shang, J.; Ai, Z.; Zhang, L. *J. Am. Chem. Soc.* **2015**, *137*, 6393–6399.

(11) Salvador, P. *J. Phys. Chem. C* **2007**, *111*, 17038–17043.

(12) Hahn, K. R.; Tricoli, A.; Santarossa, G.; Vargas, A.; Baiker, A. *Langmuir* **2012**, *28*, 1646–1656.

(13) Nakamura, R; Nakato, Y. *J. Am. Chem. Soc.* **2004**, *126*, 1290–1298.

(14) Wang, D.; Wang, H.; Hu, P. *Phys. Chem. Chem. Phys.* **2015**, *17*, 1549–1555.

(15) Sheng, H.; Zhang, H.; Song, W.; Ji, H.; Ma, W.; Chen, C.; Zhao, J. *Angew. Chemie - Int. Ed.* **2015**, *54*, 5905–5909.

(16) Paier, J.; Penschke, C.; Sauer, J. *Chem. Rev.* **2013**, *113*, 3949–3985.

(17) Nowotny, J.; Alim, M. A.; Bak, T.; Idris, M. A.; Ionescu, M.; Prince, K.; Sahdan, M. Z.; Sopian, K.; Mat Teridi, M. A.; Sigmund, W. *Chem. Soc. Rev.* **2015**, *44*, 8424–8442.

(18) Tan, S.; Ji, Y.; Zhao, Y.; Zhao, A.; Wang, B.; Yang, J.; Hou, J. G. *J. Am. Chem. Soc.* **2011**, *133*, 2002–2009.

(19) Aschauer, U.; Chen, J.; Selloni, A. *Phys. Chem. Chem. Phys.* **2010**, *12*, 12956–12960.

(20) Lee, J.; Sorescu, D. C.; Deng, X. *J. Am. Chem. Soc.* **2011**, *133*, 10066–10069.

(21) Liu, L.; Zhao, C.; Li, Y. *J. Phys. Chem. C* **2012**, *116*, 7904–7912.

(22) Li, H.; Shang, J.; Shi, J.; Zhao, K.; Zhang, L. *Nanoscale* **2016**, *8*, 1986–1993.

(23) Ye, L.; Deng, K.; Xu, F.; Tian, L.; Peng, T.; Zan, L. *Phys. Chem. Chem. Phys.* **2012**, *14*, 8–2.

(24) Li, H.; Shi, J.; Zhao, K.; Zhang, L. *Nanoscale* **2014**, *6*, 14168–14173.

(25) Jiang, J.; Zhao, K.; Xiao, X.; Zhang, L. *J. Am. Chem. Soc.* **2012**, *134*, 4473–4476.

(26) Zhao, K.; Zhang, L.; Wang, J.; Li, Q.; He, W.; Yin, J. J. *J. Am. Chem. Soc.* **2013**, *135*, 15750–15753.

(27) Dean, J. A. Lange's Handbook of Chemistry, 15th ed.; McGraw-Hill: NewYork, **1998**.

(28) Sumita, M.; Hu, C.; Tateyama, Y. *J. Phys. Chem. C* **2010**, *114*, 18529–18537.

(29) Bandura, A. V.; Kubicki, J. D.; Sofo, J. O. *J. Phys. Chem. B* **2008**, *112*, 11616–11624.

(30) Henderson, M. A. *Langmuir* **1996**, *12*, 5093–5098.

(31) Sheng, H.; Li, Q.; Ma, W.; Ji, H.; Chen, C.; Zhao, J. *Appl. Catal. B Environ.* **2013**, *138-139*, 212–218.

(32) Bates, S. .; Kresse, G.; Gillan, M. *Surf. Sci.* **1998**, *409*, 336–349.

(33) Tilocca, A.; Selloni, A. *J. Phys. Chem. B* **2004**, *108*, 4743–4751.

(34) Bikondoa, O.; Pang, C. L.; Ithnin, R.; Muryn, C. A.; Onishi, H.; Thornton, G. *Nat. Mater.* **2006**, *5*, 189–192.

(35) Wang, J.; Luo, W.; Feng, J.; Zhang, L.; Li, Z.; Zou, Z. *Phys. Chem. Chem. Phys.* **2013**, *15*, 16054–16064.

(36) Sun, C.; Liao, T.; Lu, G. Q. (Max); Smith, S. C. *J. Phys. Chem. C* **2012**, *116*, 2477–2482.

(37) Schaub, R.; Thostrup, P.; Lopez, N.; Lægsgaard, E.; Stensgaard, I.; Nørskov, J. K.; Besenbacher, F. *Phys. Rev. Lett.* **2001**, *87*, 266104.

(38) Wang, Y.-G.; Mei, D.; Li, J.; Rousseau, R. *J. Phys. Chem. C* **2013**, *117*, 23082–23089.

(39) Wendt, S.; Schaub, R.; Matthiesen, J.; Vestergaard, E. K.; Wahlström, E.; Rasmussen, M. D.; Thostrup, P.; Molina, L. M.; Lægsgaard, E.; Stensgaard, I.; Hammer, B.; Besenbacher, F. *Surf. Sci.* **2005**, *598*, 226–245.

(40) Langel, W. *Surf. Sci.* **2002**, *496*, 141–150.

(41) Cicero, G.; Catellani, A.; Galli, G. *Phys. Rev. Lett.* **2004**, *93*, 016102.

(42) Xu, L.; Wu, Z.; Zhang, W.; Jin, Y.; Yuan, Q.; Ma, Y.; Huang, W. *J. Phys. Chem. C* **2012**, *116*, 22921–22929.

(43) Teobaldi, G.; Hofer, W. A.; Bikondoa, O.; Pang, C. L.; Cabailh, G.; Thornton, G. *Chem. Phys. Lett.* **2007**, *437*, 73–78.

(44) Henderson, M. A. *Surf. Sci.* **1996**, *355*, 151–166.

(45) Szczepankiewicz, S. H.; Colussi, A. J.; Hoffmann, M. R. *J. Phys. Chem. B* **2000**, *104*, 9842–9850.

(46) Sakai, N.; Fujishima, A.; Watanabe, T.; Hashimoto, K. *J. Phys. Chem. B* **2003**, *107*, 1028–1035.

(47) Wang, R.; Hashimoto, K.; Fujishima, A.; Chikuni, M.; Kojima, E.; Kitamura, A.; Shimohigoshi, M.; Watanabe, T. *Nature* **1997**, *388* (6641), 431–432.

(48) Wang, R.; Hashimoto, K.; Fujishima, A.; Chikuni, M.; Kojima, E.; Kitamura, A.; Shimohigoshi, M.; Watanabe, T. *Adv. Mater.* **1998**, *10*, 135–138.

(49) Wang, R.; Sakai, N.; Fujishima, A.; Watanabe, T.; Hashimoto, K. *J. Phys. Chem. B* **1999**, *103*, 2188–2194.

(50) Sun, R.-D.; Nakajima, A.; Fujishima, A.; Watanabe, T.; Hashimoto, K. *J. Phys. Chem. B* **2001**, *105*, 1984–1990.

(51) Zhao, J.; Li, B.; Onda, K.; Feng, M.; Petek, H. *Chem. Rev.* **2006**, *106*, 4402–4427.

(52) Li, H.; Zhang, L. Z. *Nanoscale* **2014**, *6*, 7805–7810.

(53) Perdew, J. P.; Burke, K.; Ernzerhof, M. *Phys. Rev. Lett.* **1996**, *77*, 3865.

(54) Segall, M. D.; Lindan P. L. D.; Probert. M. J.; Pickard. C. J.; Hasnip, P. J.; Clark, S. J.; Payne, M. C. *J. Phys.: Cond. Matt.* **2002**, *14*, 2717.

(55) Vanderbilt, D. *Phys. Rev. B* **1990**, *41*, 7892.

(56) Monkhorst, H. J.; Pack, *J. D. Phys. Rev. B* **1976**, *13*, 5188.

(57) Kresse, G.; Furthmuller, *Phys. Rev. B* **1996**, *54*, 11169.

(58) Kresse, G.; Joubert, D. *Phys. Rev. B* **1999**, *59*, 1758.

Table of Contents